Microstructure, plasticity and ductility of a TNM + alloy densified by Spark Plasma Sintering

Michael Musi, Christophe Deshayes, Guy Molénat, Louise Toualbi, Benjamin Galy, Petra Spoerk-Erdely, Muriel Hantcherli, Jean-Philippe P Monchoux, Marc Thomas, Helmut Clemens, et al.

Microstructure, plasticity and ductility of a TNM$^+$ alloy densified by Spark Plasma Sintering

Michael Musi[1], Christophe Deshayes[2], Guy Molénat[2], Louise Toualbi[3], Benjamin Galy[2], Petra Spoerk-Erdely[1], Muriel Hantcherli[2], Jean-Philippe Monchoux[2], Marc Thomas[3], Helmut Clemens[1], Alain Couret[2,*]

[1] Department of Materials Science, Montanuniversität Leoben, Franz-Josef-Straße 18, 8700 Leoben, Austria

[2] CEMES, Université de Toulouse, CNRS, 29 rue Jeanne Marvig, BP 94347, 31055 Toulouse, France

[3] ONERA/DMAS, Université Paris Saclay, 29 Avenue de la Division Leclerc, BP 72, 92322 Châtillon Cedex, France

[*] Correspondence: alain.couret@cemes.fr

Abstract:

This work presents a study of the microstructure and mechanical properties of a TNM$^+$ alloy (Ti-43.5Al-4Nb-1Mo-0.1B-0.3C-0.3Si, in at.%) densified by Spark Plasma Sintering (SPS), in comparison to the as-SPSed TNM alloy which contains neither carbon nor silicon. Tensile tests at room temperature and 800°C as well as creep tests at 800°C and 200 MPa were performed. The microstructures and the fracture surfaces of deformed samples were studied by scanning and transmission electron microscopies as well as by X-ray diffraction. The deformation mechanisms were investigated by means of *in situ* straining experiments and *post-mortem* analyses of deformed samples, both performed by transmission electron microscopy. Contrary to the TNM alloy, the as-SPSed microstructure of the TNM$^+$ alloy does not contain β/β_o phase due to the incorporation of carbon. Despite the fact that iron inclusions are responsible for premature failure of some samples during tensile tests, the TNM$^+$ alloy is found to be able to deform plastically at room temperature. The incorporation of carbon and silicon leads to an increase in the creep resistance of the alloy at 800°C.

1. Introduction

The outstanding properties of intermetallic γ-TiAl based alloys meet the demanding requirements for light-weight high-temperature structural applications in the aeronautic and automotive industry [1]. A 4th generation alloy of particular success is the TNM alloy with a nominal composition of Ti-43.5Al-4Nb-1Mo-0.1B (at.%) [2,3]. Especially, this alloy is already utilized in the form of low pressure turbine blades in the so-called geared turbofan engine powering the Airbus A320neo [4]. The TNM alloying concept relies on balanced amounts of the β-stabilizing elements Nb and Mo, which, on the one hand, improve hot-workability and, on the other hand, ensure fully solidification through the β phase, thus resulting in a texture-free and chemically homogeneous microstructure [5-7]. The phase transformation pathway for the chemical composition of the TNM alloy during solidification and subsequent cooling to room temperature can be summarized as follows: L → L+β → β → α+β → α+β+γ → α+β_o+γ → α+α_2+β_o+γ → α_2+β_o+γ [8]. Due to the alloying with Nb and Mo, either the disordered body-centred cubic (bcc) β phase (A2 structure) or its ordered counterpart, the β_o phase (B2 structure), are stable at all temperatures below the liquidus temperature [8,9]. While the presence of the β phase at forging temperatures is the reason for the improved hot-workability of the TNM alloy, the β_o phase has been found to be detrimental to the creep performance [10].

Generally, extensive research on γ-TiAl based alloys has established that their mechanical properties are substantially microstructure dependent. Typical microstructural features in β-solidifying alloys such as the TNM alloy are lamellar α_2/γ colonies, borders of β_o phase and single-phase γ grains with a globular morphology [2,9]. Especially, the antagonistic requirements of sufficient room-temperature ductility and high creep resistance at elevated temperatures are met by different types of microstructures. For enhanced room-temperature ductility, a high amount of γ phase with a globular morphology is necessary, especially since this phase is considered to be the most ductile one in γ-TiAl based alloys [11,12]. On the other hand, the highest creep resistance is achieved for so-called fully-lamellar microstructures only consisting of α_2/γ colonies [2,9]. Consequently, the necessary trade-off between room-temperature ductility and high-temperature creep resistance requires a microstructure containing both lamellar colonies and globular γ grains [13]. Furthermore, the lamellar spacing within the individual α_2/γ colonies as well as their respective size have a significant influence on the ductility and creep strength [8,14].

In general, the available processing routes for γ-TiAl based alloys require additional heat treatments to achieve the suitable microstructure for the desired mechanical properties. A

powder densification technique with a high sustainability and which also allows a direct control of the material's microstructure is spark plasma sintering (SPS), which has successfully been used for different TiAl alloys [15,16]. This microstructural control, which achieves densification by simultaneously applying a pulsed electric current and uniaxial pressure, is realized by the used SPS dwell temperature [17]. Especially, the SPS microstructure can be controlled by this dwell temperature which can be chosen in different phase field regions in accordance with the corresponding phase diagram. Dwell temperatures above the γ-solvus temperature in the α phase field region yield fully-lamellar microstructures. After SPS at lower temperatures in the (α+γ) phase field region, the material also contains globular γ phase, whose fraction increases with decreasing dwell temperature [16,17]. Recent research has shown that the TNM alloy can be processed by SPS and that the resulting material exhibits excellent mechanical properties [15].

In addition to the microstructure of the material, the alloying with additional elements is of particular importance for the mechanical properties of γ-TiAl based alloys [2,3,9,18]. Two elements that have been proven to beneficially influence the resistance against creep deformation are C and Si [9,18]. Below their respective solubility limits, both C and Si act as solid solution hardening elements [19,20]. In particular, the presence of dissolved C retards the motion of dislocations and the migration of interfaces as reported in [21,22]. With sufficiently high amounts, these elements culminate into the precipitation of p-Ti_3AlC carbides and ζ-Ti_5Si_3 silicides, and therefore contribute to a further enhancement of the creep resistance [10,23-25]. Consequently, in order to improve the creep resistance of the TNM alloy, a derivative alloy, designated TNM^+, has been developed that contains additions of 0.3 at.% of both C and Si [11]. With respect to the influence of these elements on the stability of the individual phases, C has been found to strongly stabilize the α phase and to even introduce a single α phase field region in the transformation pathway of the TNM alloy for additions of more than approximately 0.1 at.% [26]. Unlike C, Si is found to stabilize the γ phase at the expense of the α/α_2 phase and to increase solid-solid phase transition temperatures [27].

In the present work, the microstructure formation is investigated during SPS and the mechanical properties of the TNM^+ alloy compared to the TNM alloy. The influence of Si and C on the solidification pathway and on the SPS microstructures are studied in details. Regarding the mechanical properties, special attention is paid to the brittleness of TNM^+ alloy.

2. Materials and Methods

The chemical compositions of the gas atomized pre-alloyed TNM and TNM$^+$ powders used are given in Table 1. The SPS densifications have been carried out on these powders at dwell temperatures of 1300 °C, 1325 °C and 1360 °C following the classical cycles described elsewhere [17]. For each experiment, the temperature rise was initially 100 K/min and then reduced to 25 K/min during the last three minutes, in order to prevent a temperature overshoot. Cylindrical samples with typical diameters of 36 mm were sintered using a constant pressure of 50 MPa and a 2 min holding time at the dwell temperature. All temperatures given in this paper are the sample temperatures, i.e. the temperature measured on the graphite matrix plus 60°C [17].

Table 1. Chemical analysis of the TNM and TNM$^+$ powder. The values are given in at.% and were determined using X-ray fluorescence spectroscopy, inductively coupled plasma optical emission spectroscopy and carrier hot gas extraction.

Alloy	**Ti**	**Al**	**Nb**	**Mo**	**B**	**C**	**Si**
TNM	51.1	43.9	4.0	0.95	0.1	-	-
TNM+	51.0	43.1	3.35	0.95	0.1	0.3	0.3

The microstructures were studied by means of scanning electron microscopy (SEM) using back-scattered electron (BSE) imaging and in transmission electron microscopy (TEM). Quantitative microstructural data were extracted from SEM micrographs by using the ImageJ software. The grain size was evaluated by considering the diameter of a circle with the same area as the grain. TEM thin foils were prepared by standard jet polishing using the A3 electrolyte commercialised by Struers at -10°C with a current of 500 mA and a voltage of 90 V. TEM investigations were performed on a JEOL 2010 operating at 200 keV. Local chemical compositions were measured by energy-dispersive X-ray spectroscopy (EDS) in the SEM and TEM (using the STEM mode for Scanning Transmission Electron Microscopy) and will be given in at. % in the following. X-ray diffraction (XRD) measurements were conducted on an AXS D8 Advance diffractometer from Bruker using CuK_α radiation. From these measurements, the volume fractions of the occurring phases were determined by Rietveld analysis utilizing the software MAUD [28].

In order to determine the microstructural evolution during the SPS densification of the TNM$^+$ alloy, heat treatments were performed on a dilatometer of type 805A/D from Thermo Fisher. This was done to precisely control the sample temperature in accordance with the

temperature profile of the SPS process as well as to quench the sample to room temperature to preserve the high-temperature microstructure. However, since the temperature is controlled with a thermocouple, material, which was pre-densified by SPS was used as the starting material for these heat treatments in contrast to the SPS process, which starts from powders. The heat treatments were conducted in an Ar5.0 atmosphere to prevent any oxygen effect on the microstructure.

The crystallographic orientations of the γ grains or lamellae were determined using the selected dark field technique [29] which is based on the use of the TEM diffraction. These orientations are identified using the crystallographic projection, which allows them to be located in relation to each other. It is recalled that six orientation variants of the γ lamellae can be found in one lamellar grain and that one of them appears to be largely predominant, as a result of the lamella precipitation process [30].

Three test specimens, suitable for tensile tests at room temperature (strain rate 10^{-4} s^{-1}) and creep experiments, were machined from each SPS processed billet. Concerning the tensile tests at room temperature, the following data were extracted from the curves of the true stress as a function of the true elongation:

- Yield strength: stress at which plastic deformation starts and defined as the stress at 10^{-3} % plastic elongation,
- R0.2: the tensile stress at 0.2 % plastic elongation,
- UTS: ultimate tensile stress, and
- A: plastic elongation at rupture.

The cross-sections of the fracture surfaces of the specimens broken during tensile tests were analysed by SEM. To observe the dislocation microstructures present in these samples, TEM thin foils were extracted from disks cut perpendicularly to the tensile axis.

3. Results

3.1 Microstructure after SPS

The as-SPSed microstructures of the TNM$^+$ and TNM alloys at dwell temperatures of 1300 °C, 1325 °C and 1360 °C are compared in Figure 1 [15]. Lamellar colonies consisting of α_2 and γ phases are the main microstructural constituent regardless of the dwell temperature and the chemical composition. These α_2/γ colonies are characterized by an equiaxed overall morphology and by serrated boundaries. The major difference between the TNM and TNM$^+$ alloys is visible at the borders of the lamellar colonies. In the case of the TNM$^+$ alloy, no β_o phase is observed and the α_2/γ colonies are separated by only γ phase. Consequently, such features are called γ borders. In contrast, additional β_o phase is distributed homogeneously at the borders of the α_2/γ colonies in the case of the TNM material for a dwell temperature of 1325 °C and 1360 °C. However, in the case of the TNM alloy densified at 1300 °C, β_o phase is only present in a few specific parts of the microstructure, arising from heterogeneities in the powder particles (Figure 1a).

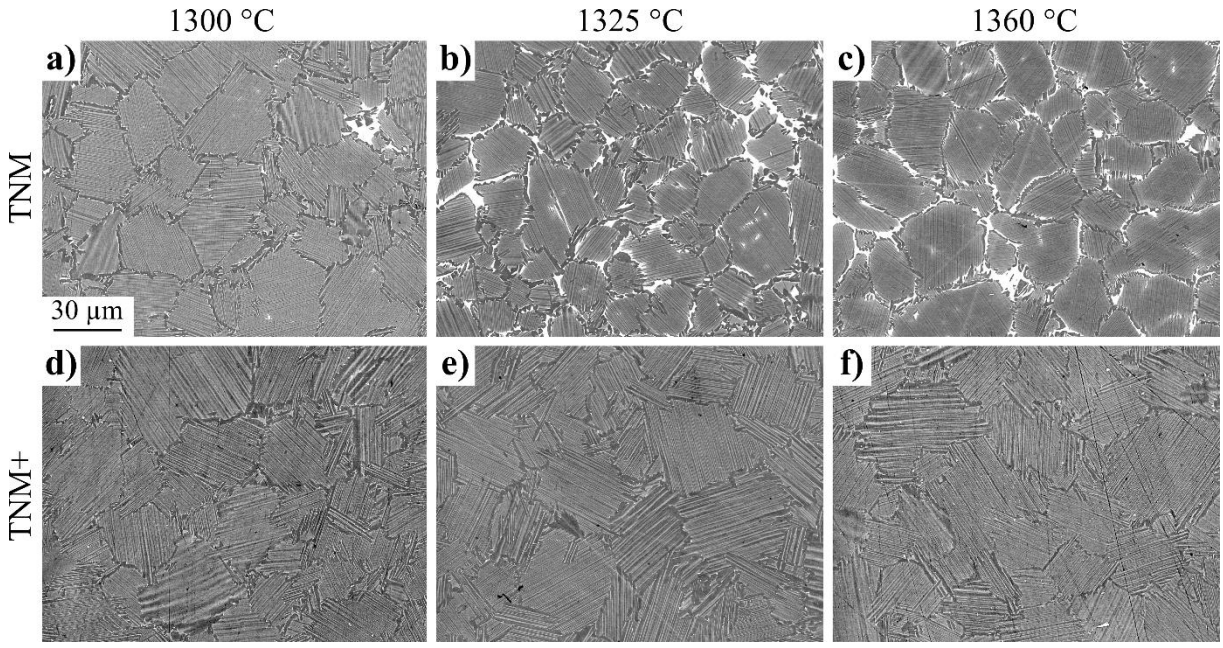

Figure 1. SEM-BSE micrographs of the microstructures obtained by SPS at dwell temperatures of 1300 °C, 1325 °C and 1360 °C, respectively, for the TNM alloy (a-c) and the TNM$^+$ alloy (d-f). The microstructures consist of γ phase (dark), α_2 phase (bright grey) and, in the case of the TNM alloy, β_o phase (white).

In order to quantitatively characterize the influence of Si and C as well as that of the SPS dwell temperature on the microstructure of the TNM based material, an image analysis of SEM micrographs was performed. The resulting values for the α_2/γ colony size and the surface fractions of the lamellar grains, γ borders and β_o phase are presented in Table 2. Since the slight variations in the measured colony sizes are within the experimental uncertainty (for instance, the standard deviation of the grain size measurements is greater than 10 µm), the colony size appears to be essentially independent of the dwell temperature in the investigated temperature range for both alloys. The surface fraction of lamellar colonies is higher for TNM$^+$ alloy, due to the absence of β_o phase at the borders.

Additionally, the volume fractions of the α_2, β_o and γ phase determined by Rietveld analysis of XRD measurements are also given in Table 2. It reveals that the phase fractions are essentially independent of the SPS dwell temperature for both TNM and TNM$^+$ alloys. However, the amount of γ phase is higher in the TNM$^+$ materials, e.g. 78 vol.% versus 71 vol.%, while the amount of α_2 phase is essentially the same, i.e. about 22 vol.%. The remaining volume fraction in the TNM alloy is occupied by the β_o phase. Although very small peaks associated with the β_o phase could also be identified in the XRD spectra of the TNM$^+$ alloy, the amounts were too small to be determined quantitatively. The presence of minor amounts of β_o phase in the TNM$^+$ alloy can be attributed to chemical heterogeneities within the initial powder. Furthermore, no peaks associated with either carbides or silicides could be detected in the XRD data.

Table 2. Quantitative characterization of the SPS materials by SEM image analysis and XRD.

Alloys		**TNM$^+$**			**TNM**		
SPS Temperature [°C]		1300	1325	1360	1300	1325	1360
SEM	α_2/γ colony size [µm]	27	26	31	21	20	20
	Fraction γ borders [%]	11	9	6	16	16	14
	Fraction β_o [%]	0	0	0	3	6	7
	Fraction lamellar colonies [%]	89	91	94	81	78	79
XRD	Volume fraction γ [vol.%]	78	78	78	71	70	72
	Volume fraction α_2 [vol.%]	21	22	21	23	22	20
	Volume fraction β_o [vol.%]	<1	<1	<1	6	8	8

The local chemical composition of the TNM and TNM$^+$ alloys consolidated at 1325°C has been measured by energy-dispersive X-ray spectroscopy (EDS) in the SEM in order to investigate the distribution of the alloying elements in the SPS microstructures and to search for possible local enrichments in Si, which might explain the presence of silicides. Note that C

cannot be detected by this experimental technique due to the usual carbon contamination of SEM and TEM samples and the difficulty of measuring the low energy edges of light elements. The resulting quantitative elemental distributions within the individual microstructural features, i.e. lamellar colonies, γ borders and β_o phase, both in the TNM and TNM$^+$ alloy are given in Table 3. The lamellar colonies are characterized by a lower Al content when compared to the γ borders, e.g. 43.6 at.% and 46.1 at.%, respectively, in the case of the TNM$^+$ alloy. This can be attributed to the fact that the lamellar colonies essentially consist of both γ phase and α_2 phase, the latter possessing a lower Al content in general and, thus, reducing the overall Al content within this microstructural feature. With respect to Nb and Mo, similar values of about 4 at.% and 1 at.%, respectively, are obtained in lamellar colonies and γ borders. In contrast to this, the β_o phase, which is only visible in the SPS microstructure of the TNM alloy, exhibits higher amounts of Nb and Mo which are β-stabilizers [5]. Generally, the observed phase compositions are in agreement with other works on the TNM alloy system, e.g. see Ref. [22]. A comparison between the TNM alloy and the TNM$^+$ alloy reveals that the chemical compositions of the lamellar colonies and the γ grains at their borders are actually very similar. The only difference is the presence of Si and C in the TNM$^+$ alloy.

STEM-EDS maps have also been recorded for the same samples. Concerning Mo and Nb atoms, very homogeneous distributions were observed in the TNM$^+$ alloy (not reproduced here), consistently with the absence of β_o phase. Regarding Si (Figure 2a), even if some very small Si-rich areas can be observed, this element is homogeneously distributed. TEM investigations allowed us to detect some very scarce silicide precipitates, as exemplified in Figures 2b and c, which show the TEM image of one of them. Table 4 shows the measured chemical compositions of the three zones circled in colour in Figure 2b. The chemical composition of zone 3 is comparable to that of ξ -silicide, as determined by atom probe [31] and reported in the same table for comparison. In particular, fairly significant and moderate local enrichments in Si and Nb are measured as well as a depletion in the Al content. Figure 2c shows the TEM micrograph of this ξ –silicide (surrounded by small arrows), which appears to be located at the interfaces of lamellar zones. Their typical lengths and widths range from 500 nm to less. It should be emphasized that these precipitates are far smaller than the critical fracture length for fracture initiation debinding, which is approximately 500 μm [32], and so are not able to induce alloy failure.

Table 3. Quantitative elemental analysis by EDS at the local scale of the TNM and TNM$^+$ alloys densified at 1325°C. The values are given in at.%.

	Alloy	Ti	Al	Nb	Mo	Si
Lamellar colonies	TNM	50.6	43.2	4.3	1	-
	TNM+	50.9	43.6	4.2	1.1	0.3
γ border	TNM	48.4	46.5	4.4	0.8	-
	TNM+	48.5	46.1	4.2	0.9	0.3
β_o phase	TNM	54.7	35.6	5.8	3.9	-
	TNM+	Phase not present				

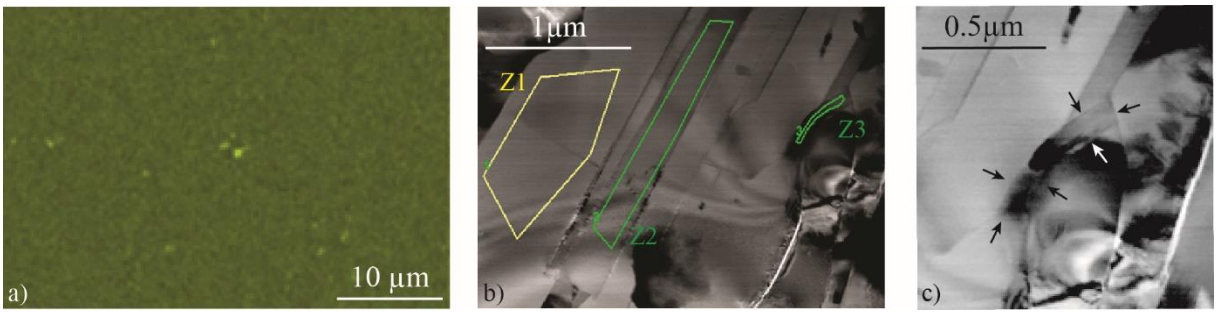

Figure 2. Study by SEM and TEM of the repartition of the Si atoms in the microstructure and within a silicide. (a) Si map by SEM of a large area; (b) delimitation of the three zones which were analysed (Table 4) and (c) TEM image of a ξ silicide precipitate.

Table 4. Quantitative elemental analysis by EDS-TEM at the local scale of three zones which are surrounded in colour in Figure2b.

	Ti	Al	Nb	Mo	Si
Zone 1	43.9	50.6	3.9	1.1	0.5
Zone 2	51.7	42.2	4.2	1.3	0.6
Zone 3	50.6	21.5	7.0	1.9	19.0
ξ-silicide [31]	50.9	13.3	9.5	0.7	21.4

Figure 3 displays a TEM study in the TNM$^+$ alloy of a γ zone (γZ) situated between two lamellar zones labelled LZ1 and LZ2, whose interface directions are perpendicular. The analysis of the border orientation based on TEM diffraction patterns has shown that its orientation is identical to that of the predominant orientation of the γ lamellae of the LZ1 lamellar zone. This result is consistent with what was previously found in the SPS-IRIS alloy [16]. However, this is a different result from that of the TNM-SPS alloy [15], in which the orientation of the γ grains at the colony boundaries are in relationship with their adjacent β_o

grain rather than with their neighbouring lamellar zones. This is emphasized in Figure 9, which shows a large zone deformed at room temperature, exhibiting several examples of such γ borders with the orientation of the neighbouring lamellae. The dark field image in Figure 3b shows that the γ border is divided into areas separated by ordered domains. Figure 3c in dark field mode shows the unique β_o precipitates of this border. The orientation of this precipitate is related to that of its surrounding γ grain, indicating that it results from a secondary precipitation, which was also the case for the heavily dense β_o precipitation observed in γ border present in the IRIS-SPS alloy [16].

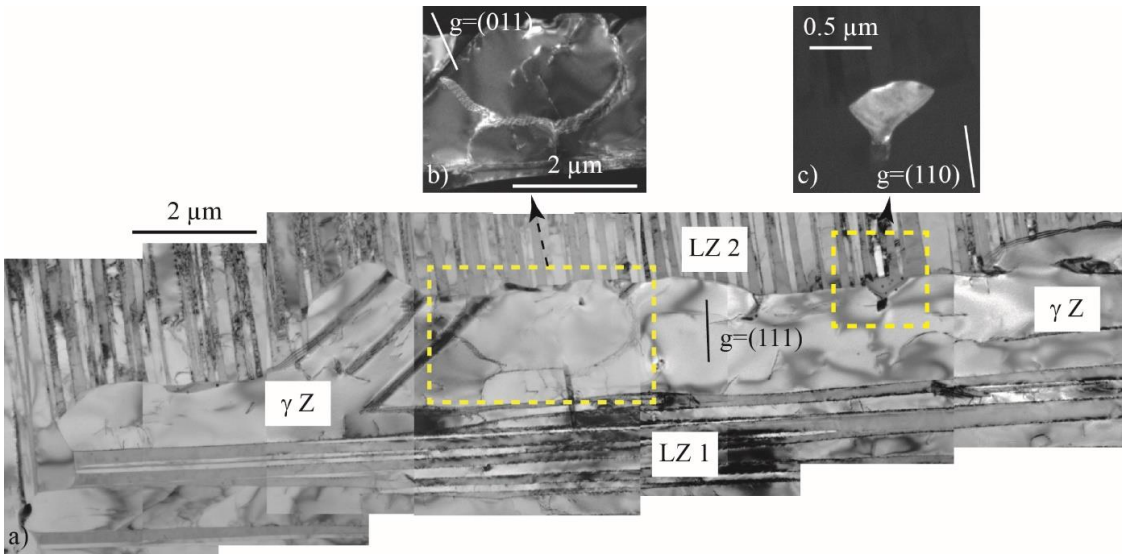

Figure 3. TEM study in TNM^+ of a γ zone (γZ) situated between two lamellar zones labelled LZ1 and LZ2. (a) General view in bright field mode; (b) ordered domain in dark field mode and (c) β_0 precipitates in dark field mode.

3.2 Microstructure after heat treatments

Heat treatments under an inert gas atmosphere were conducted to investigate both the formation of the microstructure of the TNM^+ alloy during SPS and the subsequent absence of the β_o phase as compared to the TNM alloy. The resulting microstructures of heat-treated samples are depicted in Figure 4. The performed heat treatments can be divided into two categories. Firstly, heat treatments at the SPS dwell temperatures of 1300 and 1360 °C with a holding time of 1 h followed by gas-quenching in order to determine the phases present in thermodynamic equilibrium (Figures 4a and b). Secondly, heat treatments following the temperature profile of the SPS densification with subsequent quenching of sample from specific temperatures to preserve the high-temperature microstructures (Figures 4c to e).

Comparing the microstructures of the 1 hour heat treatments at 1300 °C and 1360 °C in Figures 4a and b reveals substantial differences with respect to phases present. After the heat treatment at 1300 °C, only large α_2 grains are observed. Since this α_2 phase forms via an ordering transformation of the high-temperature α phase during subsequent water quenching from these high temperatures [30,33], it can be deduced that only the α phase is thermodynamically stable at 1300 °C. On the other hand, the heat treatment 1360 °C results in a microstructure consisting of globular α_2 grains surrounded by a mixture of α_2 laths and β_o phase, e.g. see insert in Figure 4b. Similarly to the heat treatment 1300 °C, these larger globular α_2 grains correspond to the high-temperature α phase. The mixture of α_2 and β_o at the grains boundaries and triple points of these globular grains is the remnant of the high-temperature β phase. Indeed, during water quenching, the β phase partially transforms into α laths since the $\beta \rightarrow \alpha$ transformation cannot be completely suppressed [9]. The following ordering transformation yields the observed α_2 laths. Additionally, the residual β phase from the partial $\beta \rightarrow \alpha$ transformation orders into the β_o phase. Although both the α and β phases transform into α_2 and β_o during water-quenching, a clear distinction between the high-temperature phases is possible due to the preserved chemical differences, i.e. the β phase exhibits a brighter SEM-BSE contrast due to higher amounts of Nb and Mo. Consequently, the microstructure of the material heat-treated at 1360 °C is indicative of the fact that the α phase as well as the β phase are present in thermodynamic equilibrium at this temperature. However, the β/β_o phase is not observed in the final SPS microstructure of a TNM^+ sample densified by SPS at a 1360°C dwell temperature, e.g. see Figure 1f.

In order to duplicate the temperature profile of the SPS densification, the second series of heat treatments consisted of a holding segment at 1360 °C for 5 min followed by cooling with 100 °C/min to a certain target temperature, i.e. 1200 °C and 1000 °C, and subsequent quenching to room temperature. The initial cooling rate of 100 °C/min corresponds to the average cooling rate experienced by the SPS material in this temperature regime [17]. After the holding segment of 5 min at 1360 °C (Figure 4c), the microstructure consists of α and β phases similarly to the 1 hour heat treatment. However, the amount of β phase is lower after the heat treatment with the shorter holding segment. At a temperature of 1200 °C (Figure 4d), the microstructure is predominantly made up of α grains with a minor amount of β phase still present at the triple points. It is interesting to note that the partial decomposition of the β phase into α_2 laths seems to be no more activated during cooling from 1200°C. As shown in Figure 4e, cooling to 1000 °C yields the formation of γ phase at the α/α_2 grain boundaries in a globular form as well as within the α/α_2 grains in the form of lamellae, corresponding to the γ borders and the lamellar colonies,

respectively, in the SPS microstructure. With the exception of some residual β_o phase in this heat-treated condition, the microstructure coincides with the SPS microstructure presented in Figure 1f.

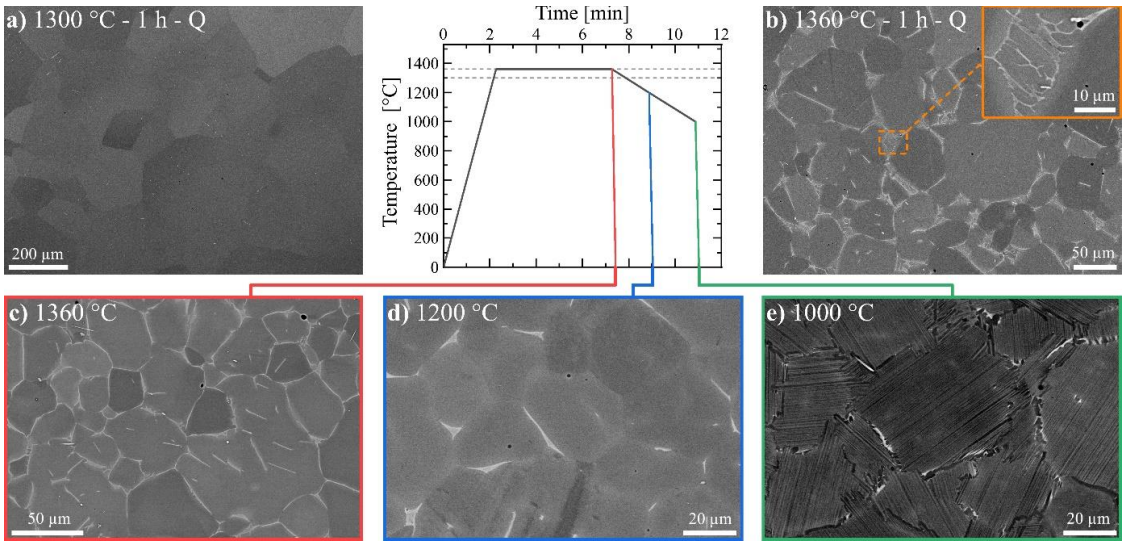

Figure 4. Microstructures of the TNM$^+$ alloy after various heat treatments: (a) and (b) correspond to 1 hour heat treatments followed by quenching; (c) to (e) quenching from specific temperatures during the reproduced SPS cycle. The temperatures given in (c) through (e) mark the respective temperatures before the quenching to room temperature, e.g. see the time-temperature curve in the centre.

3.3 Mechanical tests and fractography

The mechanical behaviour of the two examined alloys are shown in Figure 5 for various dwell temperatures, i.e. the stress-strain curves recorded at room temperature (a,b) and 800 °C (c) as well as the creep curves at 800 °C using an initial stress of 200 MPa (d). Table 5 compiles the outcomes of the tensile tests at room temperature. For all dwell temperatures investigated, the room-temperature tensile curve of the TNM$^+$ alloy is similar to the one of the TNM in the elastic domain and starts to diverge from the elastic straight line at around 500 MPa, pointing out the onset of plastic deformation. YS is slightly reduced from 560 MPa for TNM to 520 MPa for TNM$^+$ as mean values at any dwell temperature. The most significant difference between the two alloys at room temperature is that the TNM$^+$ samples fracture at a plastic strain level of less than 0.1%, while the TNM samples exhibit between 0.5 and 1% of plastic strain. The four curves obtained at room temperature for TNM$^+$ samples sintered at the same dwell temperature of 1325°C are compared in Figure 5b, showing an outstanding repeatability of the alloy properties despite this very small amount of plastic deformation. At 800°C, the TNM$^+$ alloy exhibits a lower ductility than TNM, but an increased creep resistance, as expressed by a

pronounced reduction of the minimum creep rate and a doubling of the creep life (Figure 5c and d).

Table 5. Results of tensile tests conducted at room temperature (10^{-4} s^{-1} strain rate).

	Dwell temperature		YS (MPa)	R0.2 (MPa)	UTS (MPa)	A (%)
TNM+	1300 °C	Spec 1	545		669	0.09
	1325 °C	Spec 1	553		675	0.10
		Spec 2	487		618	0.04
		Spec 3	477		590	0.04
		Spec 4	505		565	0.02
	1360°C	Spec 1	545		611	0.06
TNM	1300 °C	Spec 1	559	771	923	0.73
		Spec 2	554	759	910	0.75
	1325 °C	Spec 1	591	814	995	0.92
		Spec 2	583	792	961	0.81
		Spec 3	559	755	914	0.93
		Spec 4	545	748	905	1
	1360 °C	Spec 1	538	770	901	0.54

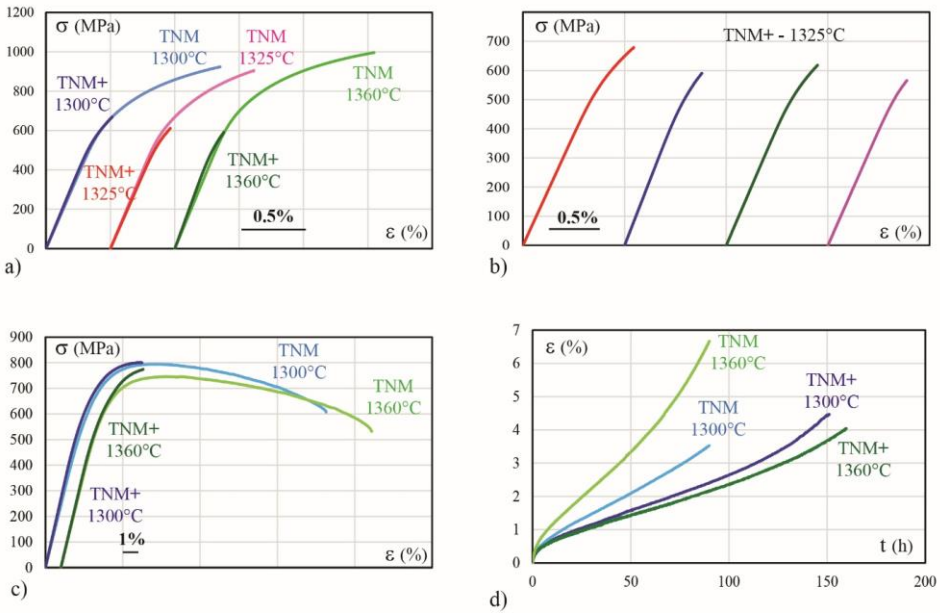

Figure 5. Mechanical properties of the TNM$^+$ and TNM alloys. a) Comparison of the tensile tests at room temperature performed on the two alloys for three different dwell temperatures; b) results of four tensile tests performed at room temperature on TNM$^+$ samples sintered at 1325 °C; (c) comparison of the tensile curves recorded at 800 °C for the TNM$^+$ and TNM alloys which were densified at different dwell temperatures; (d) creep curves at 800 °C under 200 MPa. All temperatures indicated in the diagrams are the dwell temperatures used for the densification of the corresponding material.

Both SEM fractographic and EDX chemical analysis were carried on TNM^+ tensile samples after rupture at room temperature in order to identify the origin of the low ductility of this alloy. Figure 6 shows the fracture surface of a sample sintered at a dwell temperature of 1325 °C. The SEM images obtained at different magnifications with secondary electrons allow the identification of the initiation site (marked in the dotted circle in Figure 6a) and indicate a predominantly transgranular crack propagation with the presence of facets at the lamellar interfaces (Figure 6b), as observed on TNM alloy samples [15].

Figures 6c-e display a more precise local analysis of the centre of the crack initiation site zoomed in Figure 6b. Figure 6c obtained with back-scattered electrons evidences a clear delimitated area characterized by light grey zones around a black centre. The local chemical analysis reveals that this delimitated area exhibits an enrichment in Fe, clearly visible in Figure 6d. Figure 6e indicates the presence of smaller and localized zones rich in Si. Other chemical maps not reproduced here, notably of Mo and Nb, show no evidence of other local chemical enrichments. The local chemical difference lays principally in the presence of Fe, an element not present in the nominal composition of the TNM^+ alloy and necessarily the result of a pollution introduced during the atomization process or originally present in the ingots used for the atomization. The other particularity of this particle is the black contrast in the middle, which was identified by means of SEM as cavities. Similar fracture surface investigations were performed in three other samples and in all of them such Fe contaminated areas were found as the location of the fracture initiation.

Following this observation, not deformed as-SPSed billets were examined again in the SEM. In each of the three studied billets of 36mm diameter, more than ten features similar to that identified at the origin of the failure were observed (Figure 6 f). Figure 6 f points out that this delimitated area certainly corresponds to a powder particle different from the others and that it contains some cavities. Fe and Si EDX maps have confirmed their enrichment in these species (Figure 6 g and h). The systematic observation of several of them in a billet indicate that their number is sufficiently high to be systematically present on the scale of the volume occupied by a tensile specimen. In that situation, weak points are generated that systematically lead to the premature rupture of all the specimen tested.

Concerning the explanation of the presence of the black contrast identified as cavities, two hypotheses can be put forward. They may appear during the tensile test, as the Fe-enriched particle may present a preferential embrittlement due to its locally different chemistry, or they may be due to pre-existing porosities in the initial powder particles. The observation of cavities

in the particles of non-deformed TNM samples (Figure 6 f) seems to confirm the second hypothesis. Furthermore, it is difficult to imagine how cavities can be generated at such a low elongation level in a room temperature tensile test.

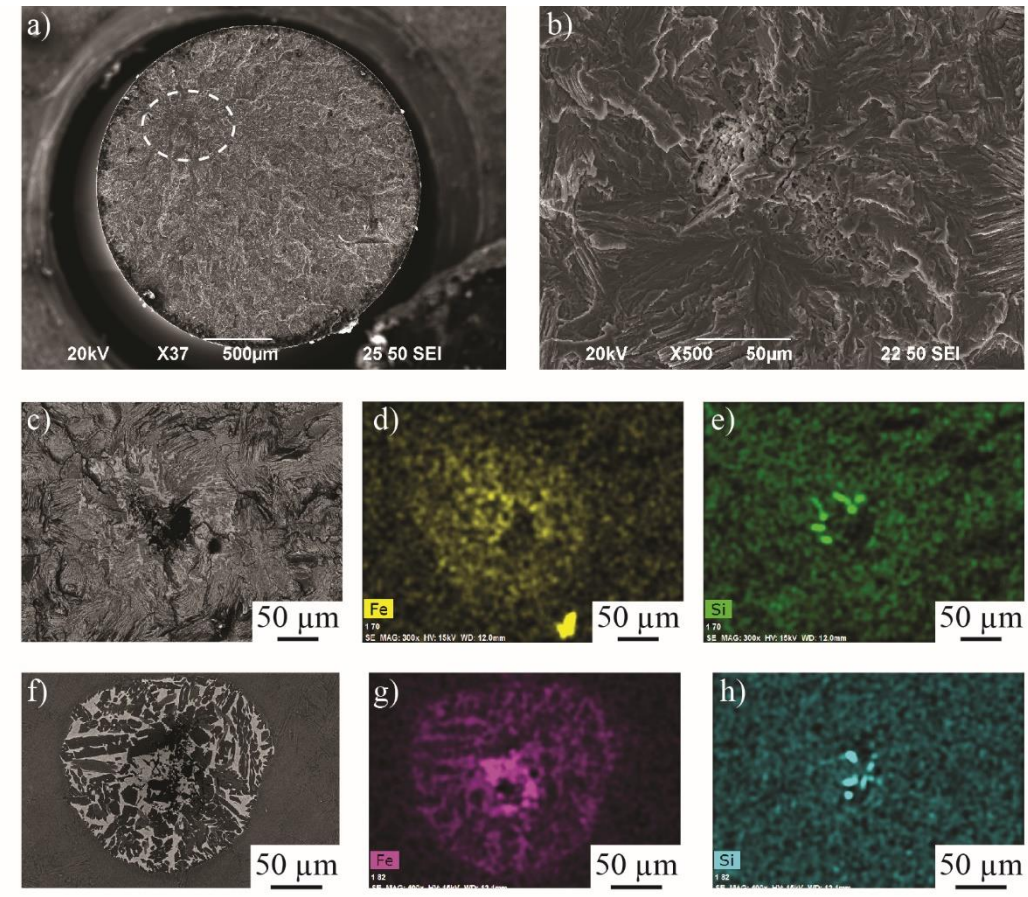

Figure 6. SEM analysis of a TNM^{+} tensile sample densified at 1325 °C after rupture at room temperature and comparison to a sample free of deformation. (a) Overview of the sample section with the crack initiation site circled; (b) enlargement of the site; (c) back-scattered electron image of the very centre of the initiation site; (d) corresponding EDX mapping of Fe; e) corresponding EDX mapping of Si; (f) contaminated particle in a not deformed as-SPSed billet; (g) corresponding EDX mapping of Fe; (h) corresponding EDX mapping of Si.

3.4 Plasticity of the γ phase

On the one hand, *in situ* deformation experiments were conducted at room temperature in a TEM and, on the other hand, thin foils extracted from specimens previously macroscopically deformed at room temperature until rupture were analysed in the TEM. The combination of these two approaches is assumed to give complementary information to qualitatively assess the

ability of the γ phase within the TNM^+ alloy to deform plastically. All these TEM investigations were performed on TNM^+ samples sintered at 1325 °C.

Figure 7 displays three sequences, (a) to (c), (d) to (g) and (i) to (m), that were extracted from the video accessible here and (h) and (m) provide complementary information. Note that for the two last sequences, the images were rotated clockwise 32° to save space. T_1 and T_2 in Figure 7a stand for two distinct pre-existing twins that were visible from the beginning of the film. They are respectively in planes $(\bar{1}11)$ and $(\bar{1}1\bar{1})$, which are almost edge-on in the plane of the micrograph. IP marks the (111) interface plane of the adjacent lamellar zone, which is inclined by 43° with respect to the plane of the micrograph. As a result, the tilted interface displays a typical contrast made of a network of interfacial dislocations that accommodate the misfit between lamellae [34]. Due to the setting out of contrast of all the dislocations by the [001] diffraction vector (picture not shown), all the dislocations that were observed to move in the sequence are ordinary dislocations. From the determination of the slip traces they left (see below), their Burgers vector was clearly determined as $b=a/2[\bar{1}10]$ (b_p is the projection of this Burgers vector in the observation plane - Figures 7a and d). One can thus see the screw character of the lengthy rectilinear segment of dislocations while the non-screw parts are curved.

The overall deformation is described in Figures 7a to c through a montage of three images collected at three distinct moments during the *in situ* tensile test. It should be emphasized that the video is continuous (there is no cutting nor editing), real-time and is an extract from a longer, multi-minute video. Between t=2 s (Figure 7a) and t=3.18 s (Figure 7b), the dislocation d_1 has not moved, but various traces such as Tr_1, Tr_2, Tr_3, or Tr_4 (marked by blue arrows in Figure 7b) were left on the surface of the sample by the passage of other dislocations. These traces were formed in a period of time that was less than the video's temporal resolution (1/25s), which indicates that the dislocations that gave rise to them are highly mobile. The signature of a slip in (111) planes is indicated by the traces Tr_1, Tr_2 and Tr_3, which are all parallel to the interface plane. The Tr_4 trace is parallel to another direction, corresponding to the trace of the $(11\bar{1})$ plane, i.e. the second slip plane which contains the Burgers vector $b=a/2[\bar{1}10]$ of the activated dislocations. The Tr_1, Tr_2 and Tr_3 traces were left by dislocations that have moved downward outside the observed area. Trace Tr_4, on the other hand, was left by the dislocation d_2 moving in the other direction, i.e. from bottom to top (Figure 7b). This is explained by cross-slip movements of the screw segments, which lead to the formation of open loops of dislocations, operating as sources which emit simultaneously upwards and downwards. These multiplication mechanisms are easily observed by examining the video. The same cross-slip movements are

also at the origin of debris left in the wake of the dislocations: six examples of them are indicated by short pink arrows in Figure 7c where new dislocations, e.g., d_3, d_4 and d_5, have also arrived in the area.

In the second sequence (Figures 7d to g), more details can be observed of the movement of one screw dislocation (d_6), leading to the formation of such a slip trace. In Figure 7d, dislocation d_6, which was previously issued from a multiplication event, appears to be elongated along its screw direction and anchored at a pinning point (green arrow). Its subsequent movement is a succession of short jumps of screw or non-screw segments. All these jumps are indicated by small orange arrows positioned on the corresponding starting positions. Between Figures 7d and e the upper screw segment jumps, leading to the formation of a non-screw one, which is still anchored at the same pinning point (green arrow in Figure 7e). Between Figures 7e and f, the two screw segments jump and the dislocation escapes from the pinning point, allowing this non-screw segment to move. Between Figures 7f and g, the whole dislocation escape and leaves the slip traces labelled Tr_5 and marked by the small blue triangles in Figure 7g. All these individual jumps occurred in less than a 1/25s as mentioned previously. This rapidity of the jumps is illustrated in Figure 7h which shows the initial and final positions of a jump of a dislocation d_7 on the same video frame, due to the remanence of the florescent screen being longer than 1/25 s.

The third sequence (Figures 7i to l) follows the glide of two non-screw dislocations, d_8 and d_9, which move also jerkily by jumps. First, between Figures 7i and j, a short segment of dislocation d_9 jumps over a short distance whereas Figure 7k displays a longer jump of dislocations d_8, showing its corresponding initial and final positions on this frame. Note that these moving non-screw segments are also anchored at some pinning points, which is exemplified in more details in Figure 7m, displaying several other examples of such non-screw dislocations anchored at pinning points (green arrows).

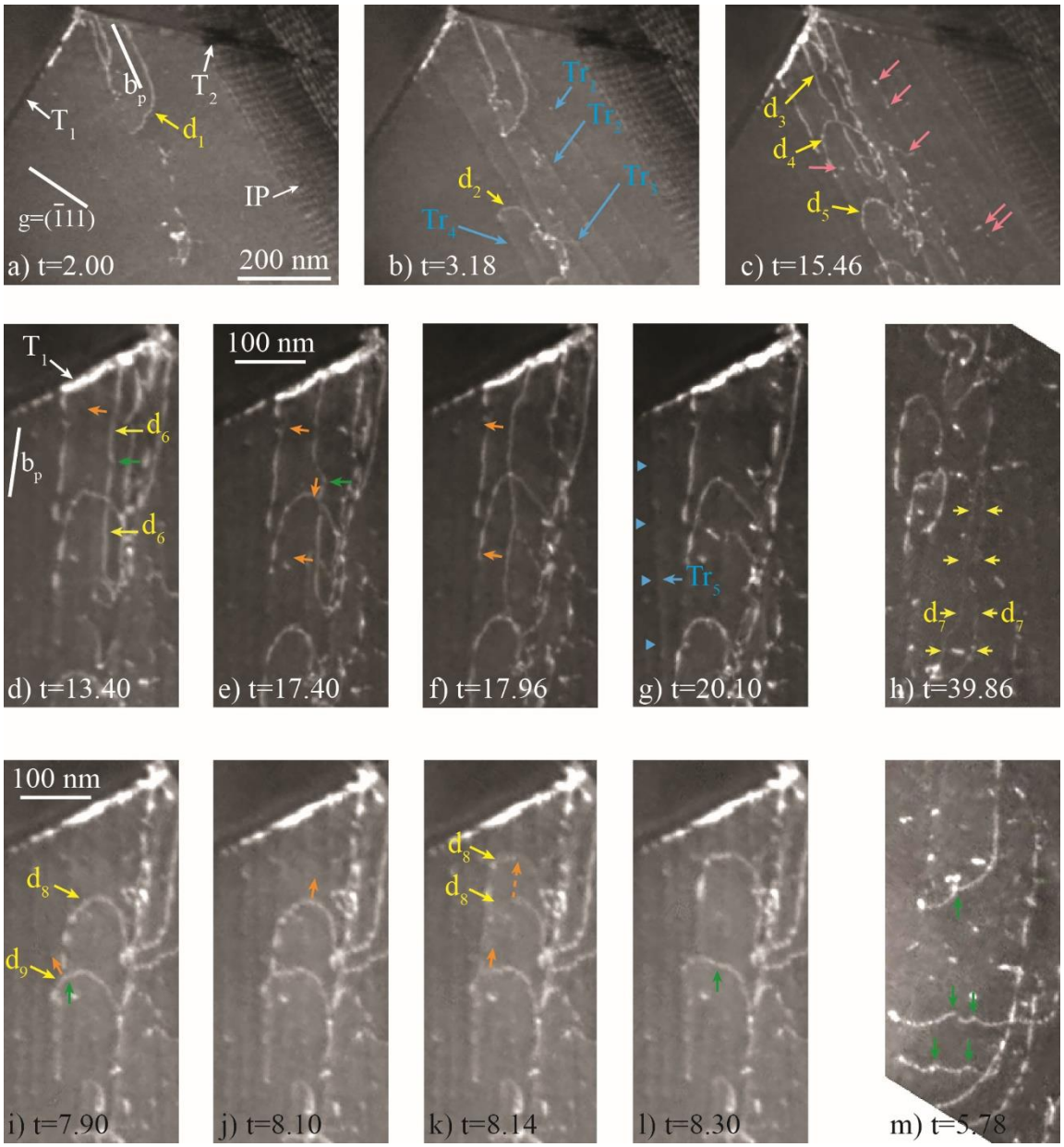

Figure 7. Movements of ordinary dislocations and formation of slip traces in the γ phase of the TNM^{+} alloy as observed by *in situ* tensile tests at room temperature in a TEM. (a) to (c) global movements of several ordinary dislocations and formation of several traces; (d) to (i) glide of a screw dislocation d_6; (h) illustration of the rapidity of the movement through the observation of the initial and final positions of a jump on the same frame; (i) to (l) glide of two non-screw dislocations d_8 and d_9; (m) pinning points on non-screw segments. g is the direction of the diffraction vector used for the images. b_p is the projection of the Burgers vector (b=a/2[$\bar{1}$10]) in the observation plane. See text for details about other indications reported in this figure and about the description of the movements. The times which are reported are those of the video.

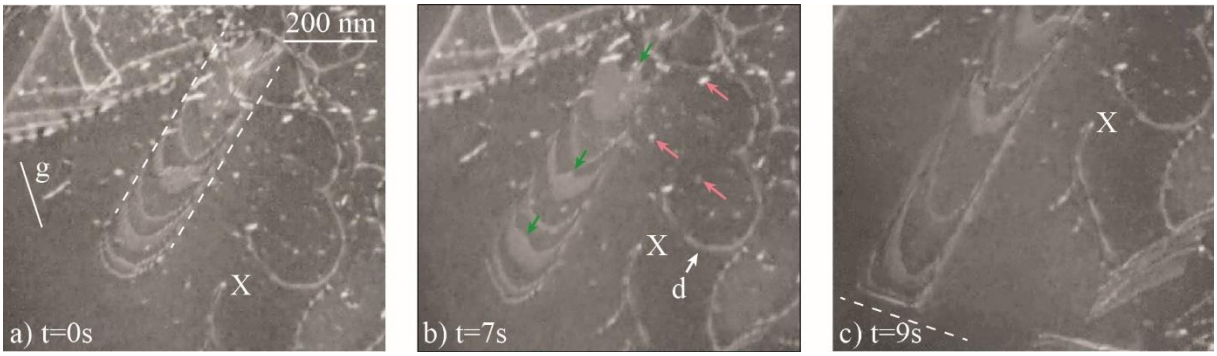

Figure 8. Progression of a mechanical twin in the γ phase of the TNM$^+$ alloy as observed by *in situ* tensile experiment in a TEM at room temperature. a) Initial situation (t=0s); b) progression of the twin; c) blocking of the twin against another out-of-contrast twin whose direction is indicated by the white dotted line.

Figure 8 is another montage from a video available here with characteristics similar to the previous one. The intersection of the plane $(\bar{1}11)$ with the sample's lower and upper surfaces is marked in Figure 8a by the two parallel dotted lines. Between these two lines, it is possible to identify the typical contrast of a twin, which consists of a series of partial Shockley dislocations that leave behind gradual contrast due to a sequence of stacking faults [35]. The first Shockley dislocation in this pile-up of dislocations is referred to as LS (Leading Shockley). At the twin tip, the distances between the first dislocations are increased with their distance to the leading one and then the dislocations become equidistant, as generally observed in TiAl[35-36]. The twin has moved downward in Figure 8b (the fixed-point X marked on the three images of the montage makes it possible to follow the evolution). The twin's motion is continuous and viscous between Figure 8a and Figure 8b (see the video), as well as between Figure 8b and Figure 8c. The Shockley dislocations are pinned at small obstacles (green arrows on Figure 8b), which were found to control the twin propagation [36]. The LS dislocation in Figure 8c is perfectly parallel to the dotted line and the twin stopped progressing because it locked onto a second twin invisible due to the diffracting vector used. Its location in a $(\bar{1}1\bar{1})$ plane is practically edge-on, whose trace is represented by the dotted line. It can be seen that debris and dislocations are present to the right of the twin, in the region above the X mark, and they do not change during the time interval covered in Figure 8. These dislocations are ordinary dislocations with dynamics identical to those observed in Figure 7. In Figure 8b, three of the debris structures are indicated by short pink arrows and one ordinary dislocation is indicated by the letter d.

These *in situ* deformation experiments have shown that the γ phase of the TNM$^+$ alloy can deform easily by twinning and glide of ordinary dislocations. Complementary TEM

investigations of the deformation microstructure in samples deformed at room temperature were performed to check the distribution of the deformation in the bulk material. Figure 9 displays the deformation spreading in a 595 μm^2 zone extracted from a TNM^+ sample. The orientations of all the γ grains were determined as described in Section 2. As recalled in Section 3.1 and exemplified in Figure 3, a lamellar grain is typically surrounded by some γ zones, which take the orientation of the predominant orientation of this grain. Considering "lamellar colonies" as the set of the lamellar grains and its satellite γ grains, the overview of this region is shown in Figure 9a. The schematic drawing in Figure 9b illustrates the state of deformation of each lamellar zone (LZ) or γ grain (γZ) following a colour code explained just below. The colours indicate the state of deformation, i.e. grey zones do not contain deformation dislocations, while zones in colour do. For the whole area depicted in Figure 9, four colonies were identified and distinguished by colour: blue for the colony 1, green for 2, purple for 3, and brown for 4. The correspondingly coloured full lines surround the whole colonies. For instance, the lamellar colony 1 contains the lamellar zone LZ1 and five γ grains, labelled from γZ1a to γZ1e. It is worth noting that 10 γ grains labelled from γZ5 to γZ14 were not found to have an orientation correlated to one of the four studied lamellar colonies; they are surrounded by a full orange line and coloured in yellow when containing some deformation dislocations. These γ grains most likely belong to lamellar zones that were removed during the preparation and, thus, are not contained within the thin foil.

The lamellar zone LZ1 and three of its five γ satellites contain some dislocations, as illustrated by their blue coloration (note: the level of blue has no significance, several shades have been used to distinguish the different areas.). No other lamellar zones, only one satellite grain (γZ2a) and four isolated γ grains (γZ5, γZ6, γZ7 and γZ14) of the 10 grains present show some marks of deformation. The white region has not been studied.

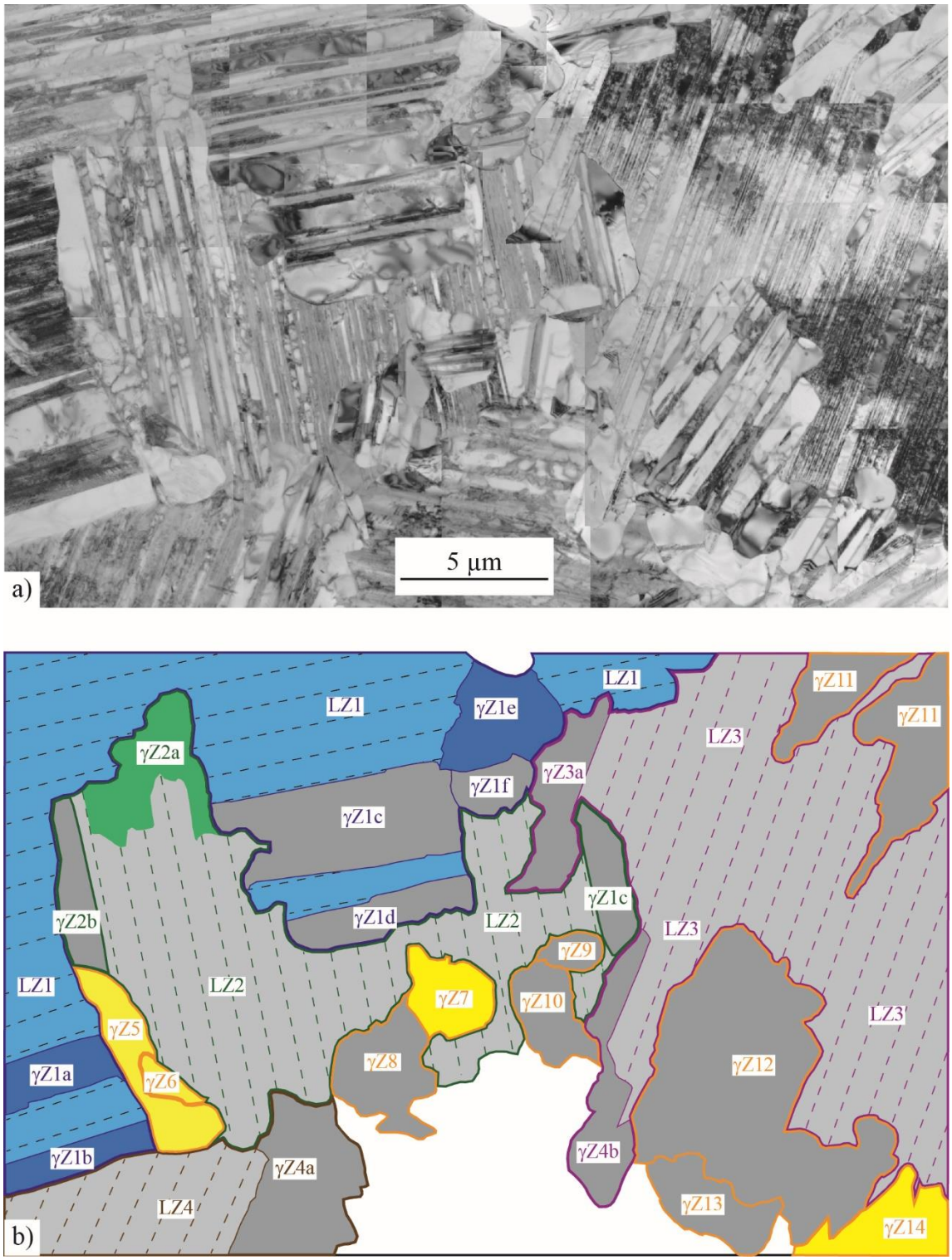

Figure 9. *Post-mortem* analysis of a 595 µm^2 area of a TNM$^+$ specimen by TEM. a) Bright field image of the area; b) schematic drawing of the same area on which is indicated the type of microstructural feature (LZ for lamellar zones, γZ for γ grains). See text for the explanation of the colour code. The white area has not been analysed.

Concerning the lamellar zones, it is interesting to note, that, by measuring the angle between the macroscopic tensile axis and the respective interface planes of the lamellar zones,

the zones LZ1 and LZ4 can be distinguished from the zones LZ 2 and LZ 3 in terms of soft and hard modes [37]: the first two are in soft mode (angles of 47º and 46º, respectively) while the other two are in hard mode (angles of 74º and 90º, respectively). This distinction is consistent with the observations of the deformation microstructure since no deformation occurs in LZ2 and LZ3. As for the two soft mode zones, LZ1 has deformed, but not LZ4, which might be less favourably oriented than LZ1 when considering the orientation of the Burgers vectors of ordinary dislocations and the tension/compression asymmetry for twinning: the low deformation of the specimen leads to a deformation which is only localized in the most favourable zones in terms of local stress and does not need to extend beyond. In this respect, the not deformed lamellar zones (LZ2, LZ3, LZ4) are twice as large as the deformed lamellar zone LZ1 (they represent 36% of the total surface studied when LZ1 represents 17%) and, in total, the deformed zones (LZ+γZ) represent 27% of the total surface studied.

Some examples of dislocations observed in the samples deformed at room temperature are displayed in Figure 10. An area with two lamellae oriented in soft modes is shown in Figures 10a and b. In Figure 10a, in which the interface plane is tilted, one dislocation loop in lamella L1 and five short dislocations in lamella L2 are marked by white arrows. In Figure 10b, the interface plane is edge-on, the diffracting vector is perpendicular to this plane and all the dislocations are out of contrast. The complete TEM analysis has shown that all these dislocations are ordinary dislocations with their Burgers vector parallel to the interface plane, thus moving in this interface plane. This situation is consistent with the soft mode for which the Schmid factor is maximum in planes parallel to the interface, allowing dislocations to propagate over long distances without encountering obstacles. Another lamella oriented in soft mode is displayed in Figure 10c for which the interfaces are inclined and the deformation occurred by mechanical twins in planes parallel to the interface plane. In Figure 10d, the deformation microstructure of a γ grain situated at a border is illustrated in which both the presence of twins and of ordinary dislocations of screw character, accompanied by a certain amount of debris, are observed.

Therefore, these *post mortem* observations and the *in situ* experiments show that the γ phase of the TNM^{+} alloy deforms at room temperature according to classical mechanisms (ordinary dislocations and mechanical twinning) and that the activation of the soft mode in the favourably oriented zones makes plasticity easy and provides all the necessary deformation systems.

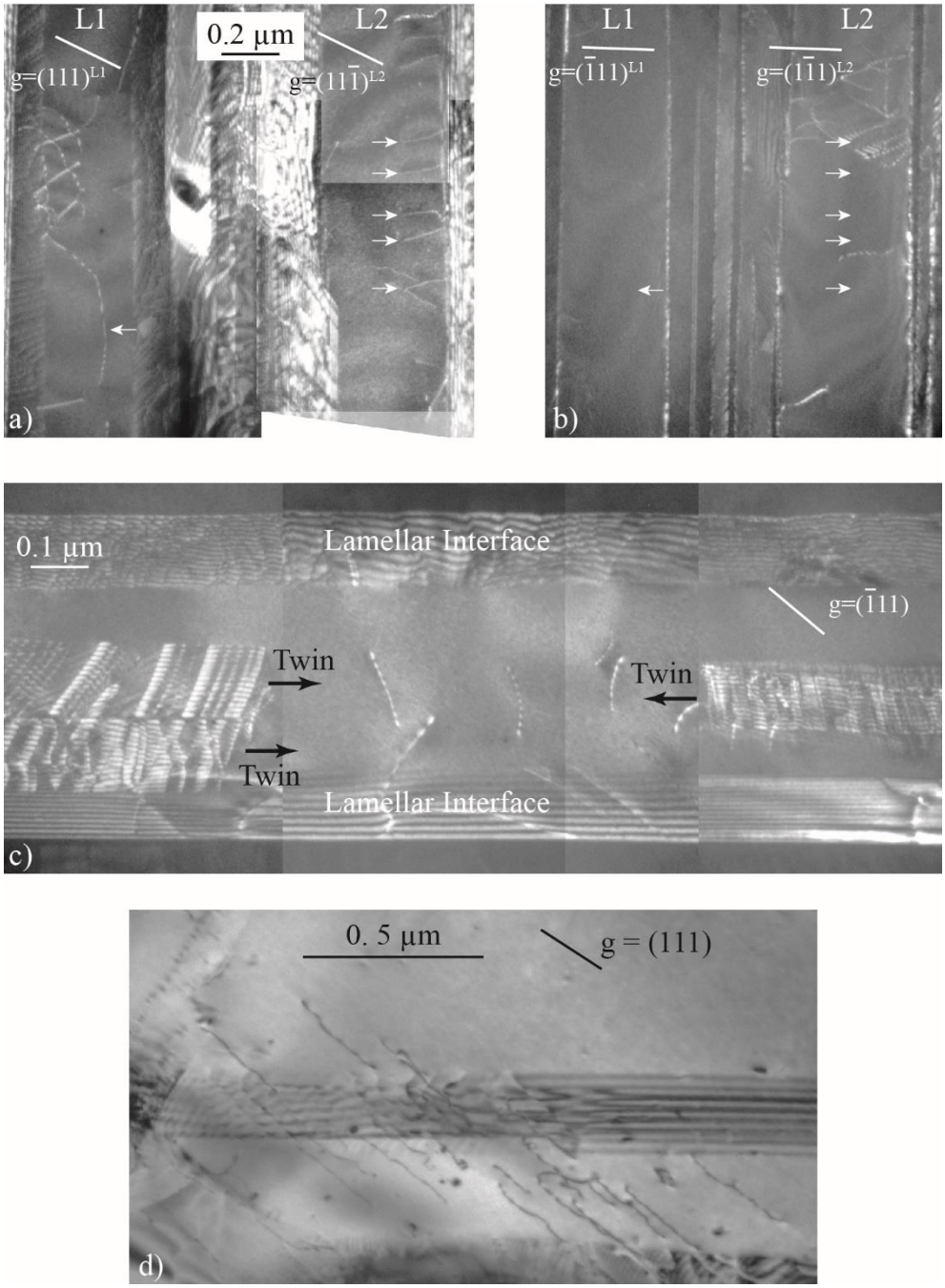

Figure 10. Several examples of deformed zones in thin foils extracted from TNM^{+} specimens which were deformed at room temperature. (a) and (b) lamellae oriented in soft mode containing some ordinary dislocations which have glided in a plane parallel to the interface plane; (c) twins in a lamella oriented in soft mode; (d) ordinary dislocations and a deformation twin in a γ zone of a border.

4. Discussion

4.1 Microstructural evolution during SPS

The main microstructural difference between the as-SPSed TNM and TNM$^+$ alloys is the almost complete absence of β_o phase in the TNM$^+$ alloy, as displayed in Figure 1. This behaviour can essentially be attributed to the alloys' chemical composition. Figure 11 shows the experimental quasi-binary phase diagram of the TNM alloying system as a function of the C content [26]. The zero C content and the red line describe the TNM and TNM$^+$ alloy, respectively. In the case of the TNM alloy, the β/β_o phase is thermodynamically stable in the temperature range of interest as predicted by the phase diagram. In case of the TNM$^+$ alloy, the situation is different. As evidenced by the microstructures after the 1 hour heat treatments shown in Figure 4a, where no β/β_o is present and only the α_2 phase is observed, a single α phase field region is present at 1300 °C. On the other hand, both the α and β phases are stable at higher temperatures, i.e. 1360 °C, consistently with the phase diagram shown in Figure 11. A similar behaviour was reported by Klein *et al.* [38], who observed the presence of an (α+β) phase field region at 1340 °C in a TNM$^+$ alloy. The presence of the α phase field region can be explained by the addition of the α-stabilizing element C in the TNM$^+$ alloy. Additionally, the higher content of α-stabilizing Al (43.1 at.%) and a lower amount of β-stabilizing Nb (3.4 at.%) of the TNM+ alloy studied in this work, compared to the TNM alloy, even further promote this particular phase field region [9]. With respect to Si, no substantial changes to the occurring phases can be expected for the contained amount of this element [27]. The relationship between the orientation of the γ border grains with that of the lamellar grains is consistent with the absence of β phase at the temperature at which the γ precursor phase starts to form. This is in contrast to the case of TNM for which the γ grain orientation was measured to be related to that of β_o grains. The situation might be similar to that of the IRIS alloy, for which correlated nucleation of the γ phase present at the borders and in the lamellar zones from the α phase was proposed to explain the final microstructure of the alloy [16].

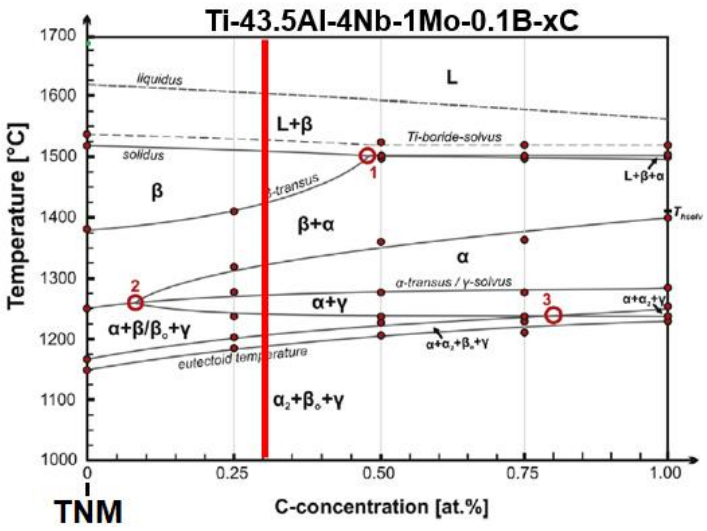

Figure 11. Quasi-binary phase diagram of the Ti-43.5Al-4Nb-1Mo-0.1B-xC (at.%) system as determined by Schwaighofer et al. [26]. The red line indicates the C content of the studied TNM$^+$ alloy. Adapted with permission from Ref. [26].

Although addition of C introduce an α and an (α+γ) phase field region, according to the phase diagram (Figure 11) the β/β$_o$ phase is stable again at lower temperatures in the TNM$^+$ alloy. However, only very few precipitates of this phase (Figures 2 and 3) can be found in the SPS microstructures of this alloy. Consequently, this almost complete absence of β$_o$ must be related to the kinetics of the associated phase transformations, i.e. the formation retardation of β/β$_o$ phase at lower temperatures, as well as a dissolution of the high-temperature β phase during cooling through the α phase field region. This fact is highlighted by the microstructures after heat treatments replicating the temperature profile of the SPS densification. In particular, the short holding time in the (α+β) phase field region is expected to reduce the amount of high-temperature β phase, when compared to thermodynamic equilibrium. Following the cooling segment at 100 °C/min during the crossing of the α phase field region, most of the β phase dissolves. The minor fraction of β phase that is still present at 1200 °C at the triple points of the α/α$_2$ grains is most likely attributed to the different starting material when compared with SPS. More precisely, the heat treatments were conducted on densified SPS material, while SPS starts from powders, which, generally, are far from thermodynamic equilibrium [39,40], thus containing high internal energy able to promote phase transformation. However, the suppression of β/β$_o$ phase formation at lower temperatures can be attributed to the slow diffusion of the β-stabilizing elements Nb and Mo, leading to a sluggish phase transformation behaviour, combined with the rather high cooling rate employed during SPS [9,17,41]. Furthermore, the SPS microstructure of the TNM alloy densified at 1300 °C, which does not

exhibit a continuous layer of β_o phase at the colony borders, can also be explained by the formation retardation of the β phase during SPS. In the case of the IRIS alloy, a secondary precipitation of β_o phase, very scarcely observed in the TNM$^+$ alloy, is activated due to a higher temperature of β/β_o transformation [16].

4.2 Plasticity and brittleness of the as-SPSed TNM+ alloy

It was established through a SEM examination of the fracture surface of the samples deformed at room temperature that Fe-rich inclusions in the TNM$^+$ alloy are responsible for the samples' early failure. Due to their size and circular shape, these inclusions were thought to be the result of Fe contamination of some of the powder particles. Similar behaviour was previously observed for a Nb containing TNB alloy that was densified by SPS, where Fe inclusions were linked with the early failure of two of a set of seven samples [42]. Due to its duplex microstructure, this TNB alloy exhibited a considerably different tensile curve at room temperature than near lamellar alloys, including the TNM$^+$ alloy: the yield strength is followed by a plateau without any hardening until the specimen breaks. The seven TNB samples had a yield strength of roughly 800 MPa. The yield strength was definitely exceeded in the tensile tests of the two samples containing Fe inclusions, and failure followed very slight plastic deformation - less than 0.1% - as it did in the current investigation. It should be emphasized that the specimens of the TNM$^+$ alloy failed at a much lower stress than those of the TNB alloy. Therefore, it appears from these two investigations that, regardless of the stress level, the onset of fracture on Fe inclusions requires a minimal amount of prior plastic deformation, whose effect is probably to produce internal stresses.

The authors of this TNB study [42] attributed the Fe contamination to impurities in the Ti sponges used to elaborate the master ingot that was later atomized. Contamination along the powder production supply chain, however, cannot be completely ruled out. The TNM$^+$ powder appears to be more contaminated than the TNB powder, for which only two out of seven samples failed early, which is consistent with the detection of several areas of Fe contamination in all SPS samples analysed after the origin of the rupture was determined. This study demonstrates the critical role that powder quality plays in producing SPS materials with high mechanical properties. In addition, a recent study of W segregations has shown the impact of the initial ingot quality for that of the final SPS product [43].

Aside from the issue of this early fracture at room temperature, plastic deformation of the TNM$^+$ alloy can be activated easily. It begins at a relatively low stress level and develops

through mechanical twinning and glide of ordinary dislocations, as seen in most TiAl alloys, particularly the as-SPSed IRIS [44] and TNM [15] alloys. Both of these systems in TNM$^+$ exhibit characteristics that are typical of TiAl alloys. The twins glide via a continuous, viscous movement of pinned Shockley dislocations, which are distributed as a pile-up at their tip and then with an equidistant distribution [35]. Ordinary dislocations which are elongated and rectilinear along their screw direction move in a jerky manner by jumps, and are anchored at small pinning points, e.g. see Ref. [45]. Furthermore, we found that in the TNM$^+$ alloy, unlike in TiAl alloys from the first generations, such as binary alloys [45], the non-screw-dislocations are anchored at the pinning sites, like in alloys containing heavy elements, such as IRIS [44] and TNM [15]. As IRIS and TNM do not contain Si and C, this pinning should result from an elastic interaction between the non-screw dislocation core and the incorporated heavy atoms, which may have segregated on the chemical clusters at their origin.

The deformation is able to spread in γ grains at the colonies' borders and in the γ lamellae of soft oriented lamellar grains. It is reasonable to expect that a TNM$^+$ alloy free of Fe inclusions will have mechanical properties at room temperature that are similar to those of the as-SPSed TNM alloy: R0.2 and UTS of nearly 800 MPa and 950 MPa, respectively, and an intrinsic limit of plastic elongation between 0.5 % and 1 %, since it has recently been shown that β_o has no detrimental effect on the brittleness of the TNM alloy [46]. The addition of C and Si appears to have no impact on the tensile properties of TNM alloys at room temperature and at 800 °C, according to the current results. However, C and/or Si seem to enhance the creep resistance, probably as a result of a change in the mobility of climbing dislocations [47], which deserves further investigation.

5. Conclusion

The microstructure and mechanical properties of a TNM$^+$ alloy (Ti-43.5Al-4Nb-1Mo-0.1B-0.3C-0.3Si (at.%)) densified by Spark Plasma Sintering were studied in this work. Based on a comparison with the behaviour of a previously investigated as-SPSed TNM alloy [15], a particular attention was paid to the influence of C and Si in the chemical composition of the alloy.

All of the experimental observations regarding microstructures match with the phase diagram of the Ti-43.5Al-4Nb-1Mo-0.1B-xC (at.%) system that was previously established [26]. The incorporation of C causes the disappearance of the β_o phase, which was explained by the existence of a single α phase field region in which the dwell temperature of the SPS cycle

is located. Despite the β/β_o phase stability at low temperature, a secondary precipitation during cooling of this phase occurs very scarcely due to the low diffusivity of Nb and Mo and to the low temperature of the corresponding structural transformation.

The tensile behaviour of the as-SPSed TNM+ alloy suffers from the presence of Fe inclusions, which reduce the alloy ductility to less than 0.1 % of plastic strain. In contrast, this alloy appears to exhibit plastic behaviour, as evidenced by a deviation of the tensile curve from the elastic straight line at about 520 MPa and in the activation of mechanical twinning and glide of ordinary dislocations in the single-phase γ grains as well as in the γ/α_2 lamellar zones oriented in soft mode. In other words, the TNM+ alloy's plastic deformation properties are comparable to those of C- and Si-free TiAl alloys, and high strength and improved elongation to fracture might be expected at room temperature by eliminating the Fe contamination. Incorporation of C and Si improves the creep resistance of the TNM^+ alloy at 800 °C and a load of 200 MPa.

Acknowledgements

This study has been conducted in the framework of the cooperative Austrian-French project "Hi-TiAl - 18-CE91-0008-01" co-supported by the French Agence Nationale de la Recherche (ANR) and the Fonds zur Förderung der wissenschaftlichen Forschung (FWF). Michael Musi is a Recipient of a DOC Fellowship of the Austrian Academy of Sciences at the Department of Materials Science, Montanuniversität Leoben.

References

[1] B.P. Bewlay, S. Nag, A. Suzuki, M.J. Weimer, TiAl alloys in commercial aircraft engines, Mater. High Temp. 33 (2016) 549–559. https://doi.org/10.1080/09603409.2016.1183068.

[2] H. Clemens, S. Mayer, Design, processing, microstructure, properties, and applications of advanced intermetallic TiAl alloys, Adv. Eng. Mater. 15 (2013) 191–215. https://doi.org/10.1002/adem.201200231

[3] S. Mayer, P. Erdely, F.D. Fischer, D. Holec, M. Kastenhuber, T. Klein, H. Clemens, Intermetallic β-solidifying γ-TiAl based alloys − From fundamental research to application, Adv. Eng. Mater. 19 (2017) 1600735. https://doi.org/10.1002/adem.201600735.

[4] U. Habel, F. Heutling, C. Kunze, W. Smarsly, G. Das, H. Clemens, Forged intermetallic γ-TiAl based alloy low pressure turbine blade in the geared turbofan, in: V. Venkatesh, A.L. Pilchak, J.E. Allison, S. Ankern, R. Boyer, J. Christodoulou, H.L. Fraser et al. (Eds.), Proceedings of the 13th world conference on titanium, TMS, Warrendale, PA, USA, 2016, pp. 1223–1227.

[5] R. Kainuma, Y. Fujita, H. Mitsui, I. Ohnuma, K. Ishida, Phase equilibria among α (hcp), β (bcc) and γ (L10) phases in Ti–Al base ternary alloys, Intermetallics 8 (2000) 855–867. https://doi.org/10.1016/S0966-9795(00)00015-7.

[6] H. Clemens, W. Wallgram, S. Kremmer, V. Güther, A. Otto, A. Bartels, Design of Novel β-Solidifying TiAl Alloys with Adjustable β/B2-Phase Fraction and Excellent Hot-Workability, Adv. Eng. Mater. 10 (2008) 707–713. https://doi.org/10.1002/adem.200800164.

[7] V. Küstner, M. Oehring, A. Chatterjee, H. Clemens, F. Appel, Analysis of the solidification microstructure of multi-component gamma titanium aluminide alloys, in: D.M. Herlach (Ed.), Solidification and crystallization, WILEY-VCH, Weinheim, 2004, pp. 250–258.

[8] E. Schwaighofer, H. Clemens, S. Mayer, J. Lindemann, J. Klose, W. Smarsly, V. Güther, Microstructural design and mechanical properties of a cast and heat-treated intermetallic multi-phase γ-TiAl based alloy, Intermetallics 44 (2014) 128–140. https://doi.org/10.1016/j.intermet.2013.09.010.

[9] F. Appel, J.D.H. Paul, M. Oehring, Gamma titanium aluminide alloys: Science and technology, WILEY-VCH, Weinheim, 2011.

[10] M. Kastenhuber, B. Rashkova, H. Clemens, S. Mayer, Enhancement of creep properties and microstructural stability of intermetallic β-solidifying γ-TiAl based alloys, Intermetallics 63 (2015) 19–26. https://doi.org/10.1016/j.intermet.2015.03.017.

[11] H. Kestler, H. Clemens, Production, processing and application of γ(TiAl)-based alloys, in: C. Leyens, M. Peters (Eds.), Titanium and titanium alloys, WILEY-VCH, Weinheim, 2003, pp. 351–392.

[12] J.D.H. Paul, F. Appel, R. Wagner, The compression behaviour of niobium alloyed γ-titanium alumindies, Acta Mater. 46 (1998) 1075–1085. https://doi.org/10.1016/S1359-6454(97)00332-7.

[13] W. Wallgram, T. Schmölzer, L. Cha, G. Das, V. Güther, H. Clemens, Technology and mechanical properties of advanced γ-TiAl based alloys, Int. J. Mat. Res. 100 (2009) 1021–1030. https://doi.org/10.3139/146.110154.

[14] Y.-W. Kim, Strength and ductility in TiAl alloys, Intermetallics 6 (1998) 623–628. https://doi.org/10.1016/S0966-9795(98)00037-5.

[15] T. Voisin, J.-P. Monchoux, M. Hantcherli, S. Mayer, H. Clemens, A. Couret, Microstructures and mechanical properties of a multi-phase β-solidifying TiAl alloy densified by spark plasma sintering, Acta Mater. 73 (2014) 107–115. https://doi.org/10.1016/j.actamat.2014.03.058.

[16] T. Voisin, J.-P. Monchoux, M. Perrut, A. Couret, Obtaining of a fine near-lamellar microstructure in TiAl alloys by Spark Plasma Sintering, Intermetallics 71 (2016) 88–97. https://doi.org/10.1016/j.intermet.2016.01.003.

[17] T. Voisin, L. Durand, N. Karnatak, S. Le Gallet, M. Thomas, Y. Le Berre, J.-F. Castagné, A. Couret, Temperature control during Spark Plasma Sintering and application to up-scaling and complex shaping, J. Mater. Process. Technol. 213 (2013) 269–278. https://doi.org/10.1016/j.jmatprotec.2012.09.023.

[18] R.M. Imayev, V.M. Imayev, M. Oehring, F. Appel, Alloy design concepts for refined gamma titanium aluminide based alloys, Intermetallics 15 (2007) 451–460. https://doi.org/10.1016/j.intermet.2006.05.003.

[19] S.W. Kim, P. Wang, M.H. Oh, D.M. Wee, K.S. Kumar, Mechanical properties of Si- and C-doped directionally solidified TiAl–Nb alloys, Intermetallics 12 (2004) 499–509. https://doi.org/10.1016/j.intermet.2004.01.004.

[20] F. Appel, U. Lorenz, M. Oehring, U. Sparka, R. Wagner, Thermally activated deformation mechanisms in micro-alloyed two-phase titanium amminide alloys, Mater. Sci. Eng. A. 233 (1997) 1–14. https://doi.org/10.1016/S0921-5093(97)00043-9.

[21] C. Scheu, E. Stergar, M. Schober, L. Cha, H. Clemens, A. Bartels, F.-P. Schimansky, A. Cerezo, High carbon solubility in a γ-TiAl-based Ti–45Al–5Nb–0.5C alloy and its effect on hardening, Acta Mater. 57 (2009) 1504–1511. https://doi.org/10.1016/j.actamat.2008.11.037.

[22] T. Klein, M. Schachermayer, F. Mendez-Martin, T. Schöberl, B. Rashkova, H. Clemens, S. Mayer, Carbon distribution in multi-phase γ-TiAl based alloys and its influence on mechanical properties and phase formation, Acta Mater. 94 (2015) 205–213. https://doi.org/10.1016/j.actamat.2015.04.055.

[23] E. Schwaighofer, P. Staron, B. Rashkova, A. Stark, N. Schell, H. Clemens, S. Mayer, In situ small-angle X-ray scattering study of the perovskite-type carbide precipitation behavior in a carbon-containing intermetallic TiAl alloy using synchrotron radiation, Acta Mater. 77 (2014) 360–369. https://doi.org/10.1016/j.actamat.2014.06.017.

[24] T. Noda, M. Okabe, S. Isobe, M. Sayashi, Silicide precipitation strengthened TiAl, Mater. Sci. Eng. A. 192 (1995) 774–779. https://doi.org/10.1016/0921-5093(94)03313-7.

[25] Y.-W. Kim, S.-L. Kim, Effects of microstructure and C and Si additions on elevated temperature creep and fatigue of gamma TiAl alloys, Intermetallics 53 (2014) 92–101. https://doi.org/10.1016/j.intermet.2014.04.006.

[26] E. Schwaighofer, B. Rashkova, H. Clemens, A. Stark, S. Mayer, Effect of carbon addition on solidification behavior, phase evolution and creep properties of an intermetallic β-stabilized γ-TiAl based alloy, Intermetallics 46 (2014) 173–184. https://doi.org/10.1016/j.intermet.2013.11.011.

[27] M. Musi, B. Galy, A. Stark, N. Schell, M. Hantcherli, J.-P. Monchoux, A. Couret, H. Clemens, P. Spoerk-Erdely, How Si affects the microstructural evolution and phase transformations of intermetallic γ-TiAl based alloys, Materialia 24 (2022) 101475. https://doi.org/10.1016/j.mtla.2022.101475.

[28] L. Lutterotti, Total pattern fitting for the combined size–strain–stress–texture determination in thin film diffraction, Nucl. Instrum. Methods B 268 (2010) 334–340. https://doi.org/10.1016/j.nimb.2009.09.053.

[29] Zghal S, Naka S, Couret A, A quantitative tem analysis of the lamellar microstructure in TiAl based alloys, Acta Metall. Mater., 45 (1997) 3005-3015. https://doi.org/10.1016/S1359-6454(96)00398-9

[30] Zghal S, Thomas M., Naka S, Finel A., Couret A, Phase transformations in TiAl based alloys, Acta Metall. Mater., 53 (2005) 2653-2664, https://doi.org/10.1016/j.actamat.2005.02.025

[31] Klein T., Rashkova B., Holec D., Clemens H, Mayern, S., Silicon distribution and silicide precipitation during annealing in an advanced multi-phase gamma-TiAl based alloy, Acta Metall. Mater., 110 (2016) 236-245. https://10.1016/j.actamat.2016.03.050

[32] Hu D., Effect of boron addition on tensile ductility in lamellar TiAl alloys, Intermetallics 10 (2002) 851-858. https://doi.org/10.1016/S0966-9795(02)00087-0

[33] Liss KD., Bartels A., Clemens H., K.-D. Liss, Bystrzanowski S., Stark A., Gerling R., Scheu C., Schreyer A., Recrystallization and phase transitions in a gamma-TiAl-based alloy as observed by ex situ and in situ high-energy X-ray diffraction, Acta Mater. 2006, 54, 3721-3735 (https://doi.org/10.1016/j.actamat.2006.04.004).

[34] G. Saada, A. Couret, Relaxation of coherency stresses by dislocations networks in lamellar g TiAl, Phil. Mag. A, 81 (2001) 2109-2120, https://doi.org/81. https://doi.org/10.1080/01418610108217137

[35] S. Farenc, A. Coujou, A. Couret, An in situ study of twin propagation in TiAl, Phil. Mag. A., 67 (1993) 127-142. https://doi.org/10.1080/01418619308207147

[36] A. Couret, S. Farenc, D. Caillard, A. Coujou, Twinning in Advanced Materials, Edited by M.H. Yoo and M. Wuttig, The Minerals, Metals & Materials Society, 316 (1994).

[37] H. Inui, MH. Oh, A. Nakamura, M. Yamaguchi, Room temperature tensile deformation of polysynthetically twinned (PST) crystals of TiAl, Acta Metall. Mater., 40 (1992) 3095-3104 https://doi.org/10.1016/0956-7151(92)90472

[38] T. Klein, B. Rashkova, D. Holec, H. Clemens, S. Mayer, Silicon distribution and silicide precipitation during annealing in an advanced multi-phase γ-TiAl based alloy, Acta Mater. 110 (2016) 236–245. https://doi.org/10.1016/j.actamat.2016.03.050.

[39] M. Kastenhuber, T. Klein, B. Rashkova, I. Weißensteiner, H. Clemens, S. Mayer, Phase transformations in a β-solidifying γ-TiAl based alloy during rapid solidification, Intermetallics 91 (2017) 100–109. https://doi.org/10.1016/j.intermet.2017.08.017.

[40] Jabbar H., Couret A., Durand L. Monchoux JP., Identification of microstructural mechanisms during densification of a TiAl alloy by spark plasma sintering, Journal of alloys and compounds, 599 (2011) 9826–9835 https:// 10.1016/j.jallcom.2011.08.008

[41] Y. Mishin, C. Herzig, Diffusion in the Ti–Al system, Acta Mater. 48 (2000) 589–623. https://doi.org/10.1016/S1359-6454(99)00400-0.

[42] H. Jabbar, J.P. Monchoux, F. Houdellier, F.P. Schimansky, F. Pyczak, M. Thomas, A. Couret, Microstructure and mechanical properties of high niobium containing TiAl alloys elaborated by Spark Plasma Sintering Intermetallics 18 (2012) 2312-2321
https://doi.org/10.1016/j.intermet.2010.07.024

[43] A. Couret, M. Allen, MW.Rackel, B. Galy, J.P. Monchoux, V. Guther, F.Pyczak, P. Sallot, M.Thomas, Chemical heterogeneities in tungsten containing TiAl alloys processed by powder metallurgy, Materiala 18 (2021) 1-10.
https://doi.org/10.1016/j.mtla.2021.101147

[44] T. Voisin, J.-P. Monchoux, M. Thomas, C. Deshayes, A. Couret, METALLURGICAL AND MATERIALS TRANSACTIONS A 47A (2016) 6097-6108
https://doi.org/10.1007/s11661-016-3801-3

[45] Couret A., An in situ study of ordinary dislocations glide in TiAl alloys Phil Mag, 79 (1999) 1977-1994

[46] G. Molénat, B. Galy, M. Musi, L. Toualbi, M. Thomas, H. Clemens, J.P. Monchoux, A. Couret. Plasticity and brittleness of the ordered β_0 phase in a TNM-TiAl alloy. Intermetallics, 151 (2022) 1-11
https://doi.org/10.1016/j.intermet.2022.107653

[47] A. Couret, J.P. Monchoux, D. Caillard, On the high creep strength of the W containing IRIS-TiAl alloy at 850 degrees C, Acta Mater. 181 (2019) 331–341
https://doi.org/10.1016/j.actamat.2019.09.056.